Clay Minerals (2026), 1–13
doi:10.1180/clm.2026.10049

Article

Multi-scale structural regulation of a low-grade mixed-dimensional attapulgite clay intergrowth for site-synergistic Pb^{2+} capture

Huan Zhang[1,2], Hang Lu[1], Zhihui Mao[1], Zongyang Liu[1], Siyuan Wang[1] and Wenbo Wang[1]

[1]Inner Mongolia Key Laboratory of Rare Earth Catalysis, College of Chemistry and Chemical Engineering, Inner Mongolia University, Hohhot, P.R. China and [2]Inner Mongolia Institute of Food Quality and Safety Inspection and Testing, Hohhot, P.R. China

Abstract

Low-grade attapulgite clay intergrowths, composed mainly of attapulgite, illite, calcite and quartz, are abundant. The intimate intergrowth among these phases buries active surfaces under inert components, limiting performance and hindering value-added utilization. Herein, a multi-scale structural regulation strategy was employed. Sieving and water washing removed inert components for compositional regulation. High-speed shearing and ultrasonic treatment broke soft agglomerates and exposed active surfaces, achieving aggregation state regulation. Controlled thermal treatment removed channel water, activated exchangeable sites and enhanced negative surface charge, thereby regulating structural and surface chemistry. These steps progressively modified the material from its macroscopic composition down to its atomic-level surface properties. After the regulation, Pb^{2+} adsorption capacity increased from 153.1 to 237.5 mg g^{-1}. The material remained effective even at pH 1 and reduced Pb^{2+} from 1000 to 0.83 μg L^{-1}, well below the World Health Organization (WHO) guideline of 10 μg L^{-1}. X-ray diffraction, X-ray photoelectron spectroscopy and quantitative cation release analysis were performed to elucidate the adsorption mechanism. Ion exchange dominated by Ca-rich mineral serves as the primary pathway. Cation exchange on silicate surfaces, forming $PbSiO_3$, provides a key supplementary contribution. Electrostatic attraction and *in situ* precipitation participate synergistically. This work establishes a theoretical foundation and offers a reagent-free, industrially feasible route for the value-added utilization of low-grade intergrown clay resources in environmental remediation.

Keywords: Adsorption; attapulgite; heavy metal; structure regulation

(Received 30 March 2026 UTC; revised 13 June 2026 UTC; accepted 29 June 2026 UTC)

Heavy metal pollution, particularly Pb^{2+} contamination in water, threatens ecological safety and human health due to its high toxicity, persistence and bioaccumulation (Cui *et al.*, 2025; Yusuf *et al.*, 2025; Zhang *et al.*, 2025a). Adsorption is widely used for heavy metal removal because of its operational simplicity, low energy consumption and environmental compatibility (Su *et al.*, 2025; Teng *et al.*, 2025; Zhu *et al.*, 2025). Among various adsorbents, natural clay minerals are attractive candidates for this purpose due to their large reserves, non-toxicity, low cost and chemical stability (Yang *et al.*, 2024; Abdel-Azim *et al.*, 2025; Luo *et al.*, 2025).

Attapulgite, a 2:1 chain-layered hydrous magnesium aluminosilicate, has drawn considerable attention in the area of heavy metal adsorption. Its unique nanochannel structure, high specific surface area, abundant surface active sites (e.g. Si–OH, Mg–OH, Al–OH) and favourable cation-exchange capacity (CEC) make it particularly promising for this purpose (Zhang *et al.*, 2023, 2025b; Tang *et al.*, 2025). Previous studies have shown that attapulgite adsorbs various heavy metal ions (Pb^{2+}, Cd^{2+}, Cu^{2+} and Co^{2+}) through ion exchange, surface complexation, electrostatic attraction and precipitation (He *et al.*, 2011; Sun *et al.*, 2021). However, most existing research has focused on purifying or chemically modifying clay minerals – *via* acid, alkali, thermal, or organic treatments – to further improve adsorption performance (Wang *et al.*, 2016; Hu *et al.*, 2025; Zhang *et al.*, 2025c).

In nature, high-grade attapulgite deposits are limited. The vast majority of such reserves are predominantly low-grade mixed-dimensional intergrowths containing attapulgite along with calcite, quartz, chlorite and illite (Zhang *et al.*, 2021a, 2024). Because these mineral phases have similar physicochemical properties and are difficult to separate, such low-grade intergrowths have long been considered low-value resources, but their potential as functional materials has been underestimated (Diop *et al.*, 2014; Shi *et al.*, 2022).

From a materials perspective, this feature of these resources creates a dual complexity. First, the composition is mixed: active components (attapulgite, calcite) coexist with inert ones (quartz), diluting overall performance. Second, the physical aggregation state is tight: mineral particles are interwoven and severely agglomerated, thereby burying active surfaces (Han *et al.*, 2022; Lu *et al.*, 2025; Liu *et al.*, 2026). This 'dilution' and 'site burial' effect is the structural origin of the poor adsorption performance of these intergrowths and a key challenge facing their high-value utilization.

Various activation methods have been developed to improve the adsorption capability of such minerals (Wang & Wang, 2016; Zhang *et al.*, 2021b; Lu & Wang, 2022). Physical activation

Corresponding author: Wenbo Wang; Email: wangwenbo@imu.edu.cn

Cite this article: Zhang H, Lu H, Mao Z, Liu Z, Wang S and Wang W (2026) Multi-scale structural regulation of a low-grade mixed-dimensional attapulgite clay intergrowth for site-synergistic Pb^{2+} capture. *Clay Minerals*, 1–13. https://doi.org/10.1180/clm.2026.10049

© The Author(s), 2026. Published by Cambridge University Press on behalf of The Mineralogical Society of the United Kingdom and Ireland.

(grinding, ultrasonication, water washing) disrupts agglomeration and increases surface area but does not alter the intrinsic mineral structure. Chemical activation (acid, alkali or salt treatment) etches surfaces and increases active sites but introduces reagents that raise costs and the environmental burden, and may also damage the crystal structure. Thermal activation removes channel and structural water and activates lattice defects, but it cannot resolve component dilution or agglomeration burial (Bal *et al.*, 2024). Moreover, existing modification studies have largely treated 'activation' as an individual process, attributing improvements vaguely to 'increased surface area' or 'more active sites' while overlooking how inert components affect the final activation effect.

Interestingly, the complexity of intergrowths carries distinct value implications across various fields. In traditional high-value applications (e.g. catalytic supports, functional fillers), multi-mineral intergrowth is a problem because obtaining high-purity single phases is difficult from such sources. For environmental adsorption, however, this complexity could become an advantage: different mineral phases provide diverse active sites (e.g. silanol groups on attapulgite, carbonate groups on calcite), and spatially interwoven phases may create 'spatially superimposed' adsorption sites where target ions interact with multiple mineral surfaces simultaneously, achieving stronger binding than any single phase. This suggests that for low-grade mixed-clay intergrowths, preserving and leveraging multi-mineral synergy rather than pursuing purification may unlock their adsorption potential.

Based on these considerations, a component-structural multi-scale regulation strategy was applied to activate low-grade mixed attapulgite clay intergrowths. This strategy proceeds progressively from composition to aggregation state, then to structure and surface chemistry. Sieving and water washing first remove inert components such as quartz. High-speed shearing and ultrasonic treatment then break soft agglomerates and expose active surfaces (Huang *et al.*, 2026). Finally, controlled thermal treatment removes channel water from attapulgite, activates exchange sites on silicate surfaces and increases surface negative charge (Wang *et al.*, 2025a).

Systematic characterization – covering composition, aggregation state, crystal structure and surface chemistry at each stage – along with quantitative Pb^{2+} adsorption evaluation, serves three purposes: (1) to elucidate the structural evolution of low-grade mixed-clay intergrowths during multi-scale regulation; (2) to clarify the synergistic Pb^{2+} adsorption mechanism on the activated material; and (3) to demonstrate a sustainable route to obtaining high-performance adsorbents. The raw materials are natural and abundant, requiring no purification. The production process uses no chemicals, emits no chemical waste and consumes only electricity – increasingly from renewable sources. The process also lends itself to high automation, low equipment wear and batch continuous production. Abundant low-grade intergrown clay resources thus find a theoretical basis for environmental remediation. The multi-scale regulation approach may extend to other low-grade intergrown minerals. The observed calcite-dominated ion exchange also suggests a new way to exploit the adsorption potential of associated carbonate minerals in low-grade clay resources.

Experimental

Materials and reagents

Natural mixed-dimensional attapulgite clay (NC) with a particle size ≤75 μm was obtained from Ordos City, Inner Mongolia, China. Lead nitrate ($Pb(NO_3)_2$, ≥99%), nitric acid (HNO_3, guaranteed reagent (GR), 65–68%), hydrofluoric acid (HF, 40%), sodium hydroxide (NaOH, GR), sodium chloride (NaCl, analytical reagent (AR)), potassium chloride (KCl, AR), anhydrous calcium chloride ($CaCl_2$, AR) and magnesium chloride ($MgCl_2$, AR) were purchased from Shanghai Aladdin Biochemical Technology Co., Ltd (China). Deionized water (DW) was produced using a Milli-Q® Integral 10 laboratory water purification system. A lead single-element standard solution (1000 μg mL^{-1}) was obtained from the National Analysis and Testing Center for Nonferrous Metals and Electronic Materials (China).

Surface water samples were collected from the Yangtze River in Nanjing, Jiangsu (marked as YRW), the Yellow River in Baotou, Inner Mongolia (HRW) and seawater from Tianjin (SW). Tap water (TW) was collected in Hohhot, Inner Mongolia. A small volume of high-concentration Pb^{2+} solution was added to each water sample to achieve a nominal Pb^{2+} concentration of ∼1000 μg L^{-1} (exact concentrations determined by measurement). The samples were then shaken and filtered through 0.45 μm filter membranes to obtain artificially contaminated surface water samples. The physicochemical parameters of these water samples were measured as follows: pH and total dissolved solids (TDS) were determined using electrode methods (pH meter FE28 and conductivity meter FE38, METTLER TOLEDO, Switzerland); and metal element concentrations were measured by inductively coupled plasma optical emission spectrometry (ICP-OES; Avio 200, PerkinElmer, USA). The results are presented in Table S1.

Preparation of activated mineral adsorbents

Mechanical activation (compositional and aggregation state regulation)

NC was mixed with DW at a mass ratio of 15:85 and stirred for 10 min to form a slurry. The slurry was passed through a 300 mesh sieve (≈ 48 μm). The retained fraction, mainly inert components such as quartz sand, was discarded. Approximately 500 g of the sieved slurry was then stirred at 10 000 rpm for 10 min using a high-speed mixer, followed by ultrasonication for 10 min (JY98-IIIDN, ultrasonic homogenizer, Shanghai Huxi Industry Co., Ltd, China; horn diameter: 20 mm; working power: 960 W; operating in 5 s on/5 s off cycles). The treated slurry was separated by centrifugation. The solid was dried, crushed and sieved through a 200 mesh sieve (≈ 75 μm). The resulting mechanically activated sample was designated as FNC.

Thermal activation (structural and surface chemical regulation)

FNC was transferred to a muffle furnace, heated to 600°C at 10°C min^{-1}, held for 2 h and then naturally cooled to room temperature. The product was passed through a 200 mesh sieve (≈ 75 μm) and designated as FTNC. This thermal treatment removes channel water from attapulgite, activates cation-exchange sites and enhances negative surface charge. Additional characterization details are provided in the Supplementary Material.

Single-factor static adsorption experiments and model fitting

The effects of thermal activation temperature (300–900°C) and time (1–10 h) on maximum adsorption capacity were examined at a constant heating rate of 10°C min^{-1}. A Pb^{2+} solution (200 mg L^{-1}) was prepared by dissolving $Pb(NO_3)_2$ in DW and adjusted to pH 5.5. An aliquot of 20 mL of this solution was transferred to a 50 mL

https://doi.org/10.1180/clm.2026.10049 Published online by Cambridge University Press

polypropylene centrifuge tube, and 0.01 g of adsorbent powder was added. The tube was sealed and shaken in a constant-temperature incubator at 25°C for 4 h. The Pb^{2+} concentration in the supernatant was then measured. Adsorption capacity (q, mg g^{-1}) and removal efficiency (R, %) were calculated using Equations 1 & 2, respectively.

$$q = \frac{(C_0 - C_e) \times V}{m} \quad (1)$$

$$R = \frac{(C_0 - C_e)}{C_0} \times 100\% \quad (2)$$

where C_0 (mg L^{-1}) is the initial Pb^{2+} concentration, C_e (mg L^{-1}) is the equilibrium concentration, V (mL) is the solution volume and m (g) is the adsorbent mass.

Using the same procedure, single-factor experiments were conducted to investigate the effects of initial pH, initial metal ions concentration, contact time and temperature on adsorption capacity. Adsorption isotherms were fitted with the Langmuir (Equation S1; Langmuir, 1918; Abujayyab *et al.*, 2025), Freundlich (Equation S2; Amor *et al.*, 2025) and Temkin (Equation S3; Temkin & Pyzhev, 1940; Wang *et al.*, 2025b) models. Kinetic data were analysed using pseudo-first-order (Equation S4) and pseudo-second-order (Equation S5) models. Thermodynamic parameters, including Gibbs free energy change (ΔG), enthalpy change (ΔH) and entropy change (ΔS), were calculated from the temperature-dependent adsorption data using linear fitting (Equations S6–S9). All model equations are provided in the Supplementary Material.

Adsorption efficiency evaluation experiments and adsorbate elution

For high-concentration Pb^{2+} adsorption, a Pb^{2+} solution (400 mg L^{-1}; pH 5.5 ± 0.1, adjusted with dilute HNO_3 or NaOH) was used. Various adsorbent dosages (0.5–3.0 g L^{-1}) were added and shaken at 25°C for 4 h. Removal efficiency was calculated using Equation 2.

For low-concentration Pb^{2+} adsorption, a Pb^{2+} solution (1000 µg L^{-1}; pH 5.5 ± 0.1) was mixed with adsorbent at 1.0 g L^{-1} and shaken at 25°C for 0–24 h. The residual Pb^{2+} concentration in the supernatant was measured.

The Pb^{2+}-saturated adsorbent was collected, washed with DW and dried. A 0.1 g portion of the dried sample was added to 50 mL of dilute HNO_3 at varying concentrations and stirred continuously for 2 h. After elution, the solid and liquid phases were separated by vacuum filtration. The solid was washed with DW, and the combined liquid fractions were diluted to 100 mL for Pb^{2+} concentration measurement. The solid was then completely digested using a HF–HNO_3–$HClO_4$ mixture under heating, and the Pb^{2+} concentration in the digestate was measured. Total Pb content was the sum of Pb in the liquid and solid fractions. Elution efficiency was calculated from the proportion of Pb remaining in the solid phase relative to total Pb, allowing identification of optimal elution conditions.

Removal of low-concentration Pb^{2+} from actual water samples

Water samples included DW, TW, YRW, HRW and SW. Each sample was spiked with Pb^{2+} to a nominal concentration of ~1000 µg L^{-1}, thoroughly shaken and filtered through 0.45 µm filter membranes. The three adsorbents (NC, FNC, FTNC) were then applied to these contaminated samples. Residual Pb^{2+} concentration in the supernatant was measured to evaluate purification performance.

Quantitative analysis

After adsorption, the mixture was filtered through a 0.45 µm syringe filter. The filtrate was diluted with 5% HNO_3 as needed. Pb^{2+} concentration was determined by flame atomic absorption spectrometry (FAAS) for concentrations ≥1 mg L^{-1} (standard curve method, $R^2 \geq 0.999$) or by inductively coupled plasma mass spectrometry (ICP-MS) for concentrations <1 mg L^{-1} (online internal standard calibration, standard curve method, $R^2 \geq 0.996$). The concentrations of other soluble elements (Na, K, Mg, Ca, Si, Al and Fe) were measured by ICP-OES after solid–liquid separation and acidification.

Results and discussion

Structural regulation by combined mechanical and thermal activation

Raw low-grade attapulgite clay intergrowth (NC) shows three structural limitations: dilution of active components by inert minerals, burial of active surfaces by soft agglomerates and low specific surface area. A two-step activation – mechanical water-washing disaggregation followed by thermal treatment – was applied to progressively reconstruct the material structure.

Mechanical dispersion: removal of inert components and exposure of active surfaces

Mechanical disaggregation (water washing, high-speed stirring, ultrasonication) was first applied. Scanning electron microscopy (SEM) images of NC (Fig. 1a,b) show rod-like, flaky and blocky particles, corresponding to attapulgite, chlorite, calcite and quartz – a morphology typical of closely intergrown multi-mineral phases. Pronounced soft agglomeration and densely packed large aggregates are visible, indicating that the physical aggregation state causes functional dilution of active components (attapulgite, chlorite, calcite) by inert components (quartz) and burial of active surfaces. Transmission electron microscopy (TEM) images (Fig. 1c) further confirm the presence of rod-like crystals and their bundles, with significant particle agglomeration.

After mechanical treatment, soluble salts were removed. The shear stress from high-speed stirring combined with ultrasonication-induced micro-vibrations partially disrupted particle agglomeration, disintegrating dense, large aggregates (Fig. 1d,e). The resulting sample was designated FNC. Comparative TEM images (Fig. 1f) show significantly improved dispersion of rod-like crystallites and their bundles in FNC, indicating that water washing and mechanical activation reduce particle agglomeration and increase mineral dispersion.

Mineral composition changes were characterized by X-ray diffraction (XRD) and X-ray fluorescence (XRF) analyses. XRD traces (Fig. 2a) confirm the multi-mineral composition of NC, with characteristic diffraction peaks matching quartz (Joint Committee on Powder Diffraction Standards (JCPDS) No. 46-1045; Fan *et al.*, 2025), calcite (JCPDS No. 47-1743; Ali *et al.*, 2025), illite (Kadir *et al.*, 2025) and attapulgite (JCPDS No. 29-0855; Chen *et al.*, 2025). After high-speed stirring, the quartz peak intensity at 26.6°2θ decreased in FNC, indicating partial removal of quartz impurities. A strong diffraction peak near 50.6°2θ in NC disappeared after treatment, probably due to removal of soluble sodium silicates. XRF quantitative analysis (Table S1) shows that Na_2O content decreased from 0.82% to 0.38%, confirming the removal of soluble salts. The normalized SiO_2 content remained at ~51.3% after water washing.

https://doi.org/10.1180/clm.2026.10049 Published online by Cambridge University Press

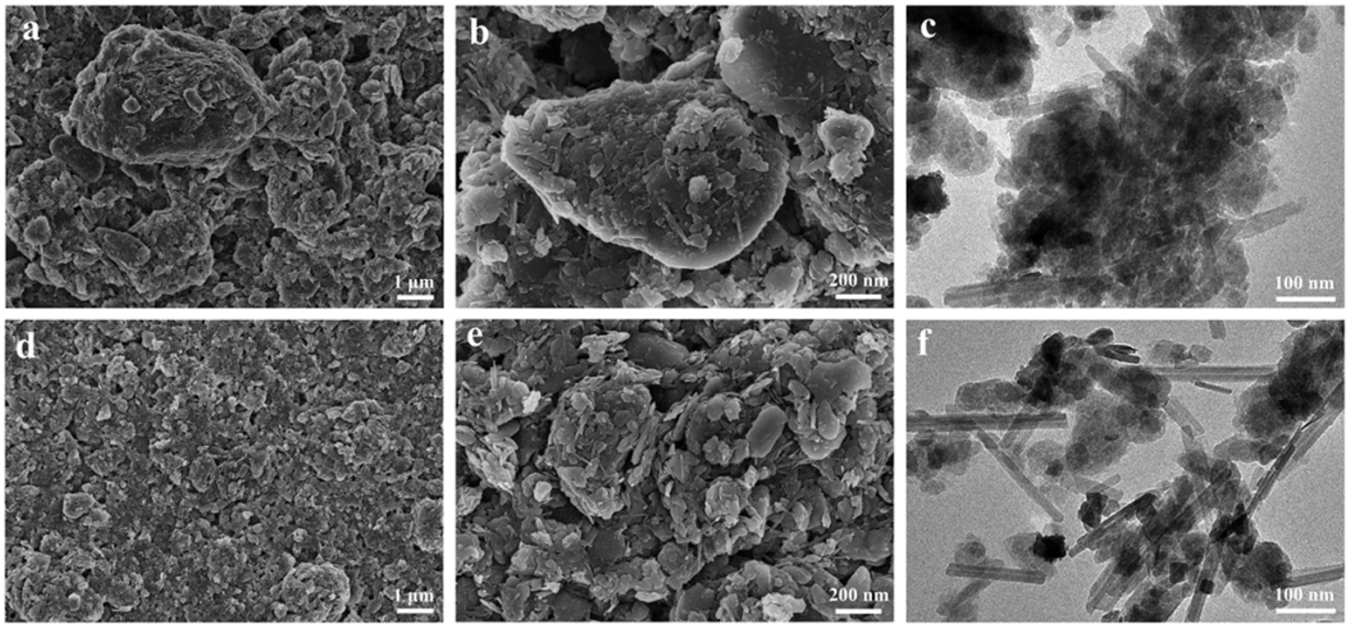


Figure 1. SEM images of (a,b) NC and (d,e) FNC; TEM images of (c) NC and (f) FNC.

Fourier-transform infrared (FTIR) spectra (Fig. 2b) further confirmed these compositional changes. The FTIR spectrum of NC show an O–H stretching vibration near 3620 cm^{-1} (internal water or hydroxyl groups in silicates), a Si–O stretching vibration at 1084 cm^{-1} (SiO_4 tetrahedra; Zhou *et al.*, 2025) and C=O stretching near 1795 cm^{-1}. Carbonate-related bands appeared at 1420 cm^{-1} (CO_3^{2-} antisymmetric stretching) and 522 cm^{-1} (out-of-plane rocking; Peng *et al.*, 2025). Quartz gives Si–O–Si symmetric stretching bands at 798 and 779 cm^{-1} and a characteristic band at 460 cm^{-1}. After treatment, the quartz-related bands (798, 779 and 522 cm^{-1}) were weakened in FNC, consistent with the XRD results.

X-ray photoelectron spectroscopy (XPS) survey spectra (Fig. 2c) show no significant differences among the three samples, as expected for physical activation. In NC, the C 1s core-level spectrum (Fig. S1) shows a peak at 289.4 eV. Ca exists in two chemical forms: carbonate (calcite) and calcium in silicate/aluminosilicate minerals. The Ca 2p spectrum (Fig. 2d) resolves two components: Ca–OC at 347.0 and 350.1 eV (Sosulnikov & Teterin, 1991) and Ca–O(Si/Al) at 351.1 and 353.4 eV (Seyama & Soma, 1984). The O 1s spectrum (Fig. 2e) show three oxygen species: Si–O–Si in quartz at 532.5 eV, Si/Al-O*M* (*M* = Mg, Fe, Ca, Na) in silicate or aluminosilicate at 531.6 eV and carbonate oxygen at 531.2 eV (Wang *et al.*, 2021). The Si 2p spectrum (Fig. 2f) shows peaks at 103.0 eV (Si–O bonds in quartz) and 102.2 eV (Si–O–*M* bonds in silicates). After treatment, the O 1s peak at 532.5 eV decreases in FNC (Fig. 2e), and the Si 2p peaks at 103.0 eV (Si 2p) and 103.7 eV (Si 2p) also decrease (Fig. 2f), indicating removal of larger quartz particles.

Mechanical disaggregation thus partially removes inert quartz and soluble salts, increasing the relative content of active phases (attapulgite, chlorite, calcite), and disrupts soft agglomerates to expose active surfaces.

Thermal activation

On the basis of the optimized composition and aggregation state, controlled thermal treatment was employed to regulate structure and surface. Calcination conditions were first optimized using the Pb^{2+} adsorption capacity of FTNC (Fig. 3a,b). At a holding time of 2 h, adsorption capacity increases with temperature from 300°C to 600°C, reaching a maximum of 219.4 mg g^{-1} at 600°C, then drops sharply to 30.1 mg g^{-1} at 900°C. At 600°C, extending the holding time from 1 to 10 h gives a maximum of 225.7 mg g^{-1} at 2 h. Below 600°C, removal of channel water from attapulgite and lattice distortion of calcite activate adsorption sites. Above 800°C, calcite decomposition ($CaCO_3 \rightarrow CaO + CO_2$) eliminated the dominant carbonate active phase. The optimal conditions are therefore 600°C and 2 h.

XRD traces after thermal activation (Fig. 2a) show reduced intensities of calcite (29.4°2θ) and attapulgite (8.5°2θ), but no disappearance, indicating that 600°C is insufficient to decompose $CaCO_3$ but may cause partial amorphization (Zunino *et al.*, 2020). Zeolitic and bound water in attapulgite are removed while the mineral framework is preserved (Boudriche *et al.*, 2012). The normalized silicon content increased by ~1% (Table S1), probably due to loss of other components (water, CO_2) during heating rather than actual Si enrichment.

FTIR spectroscopy analysis (Fig. 2b) shows weakened silicate (1084 cm^{-1}) and carbonate (1420 cm^{-1}) bands in FTNC, consistent with the XRD results. XPS analysis provided evidence of lattice distortion and site activation. In the C 1s spectrum (Fig. S1), the signal at 289.4 eV decreases in FTNC. After activation, the Ca 2p binding energy shifts by +1.2 eV (Fig. 2d), which could increase Ca ion-exchange activity. In the O 1s spectrum (Fig. 2e), the Si/Al-OM peak (531.6 eV) decreases and shifts by +0.2 eV, suggesting thermal-induced lattice distortion that may generate defects and activate reactive sites. The carbonate peak at 531.2 eV shifts by –0.1 eV with little intensity change, indicating lattice distortion without decomposition. In the Si 2p spectrum (Fig. 2f), the silicate peak at 102.2 eV shifts by +0.2 eV, further confirming this lattice distortion.

Thermal activation at 600°C thus induces lattice distortion in attapulgite and calcite without phase decomposition while removing channel water to clear pores. These effects activate reactive sites while preserving the mineral framework.

https://doi.org/10.1180/clm.2026.10049 Published online by Cambridge University Press

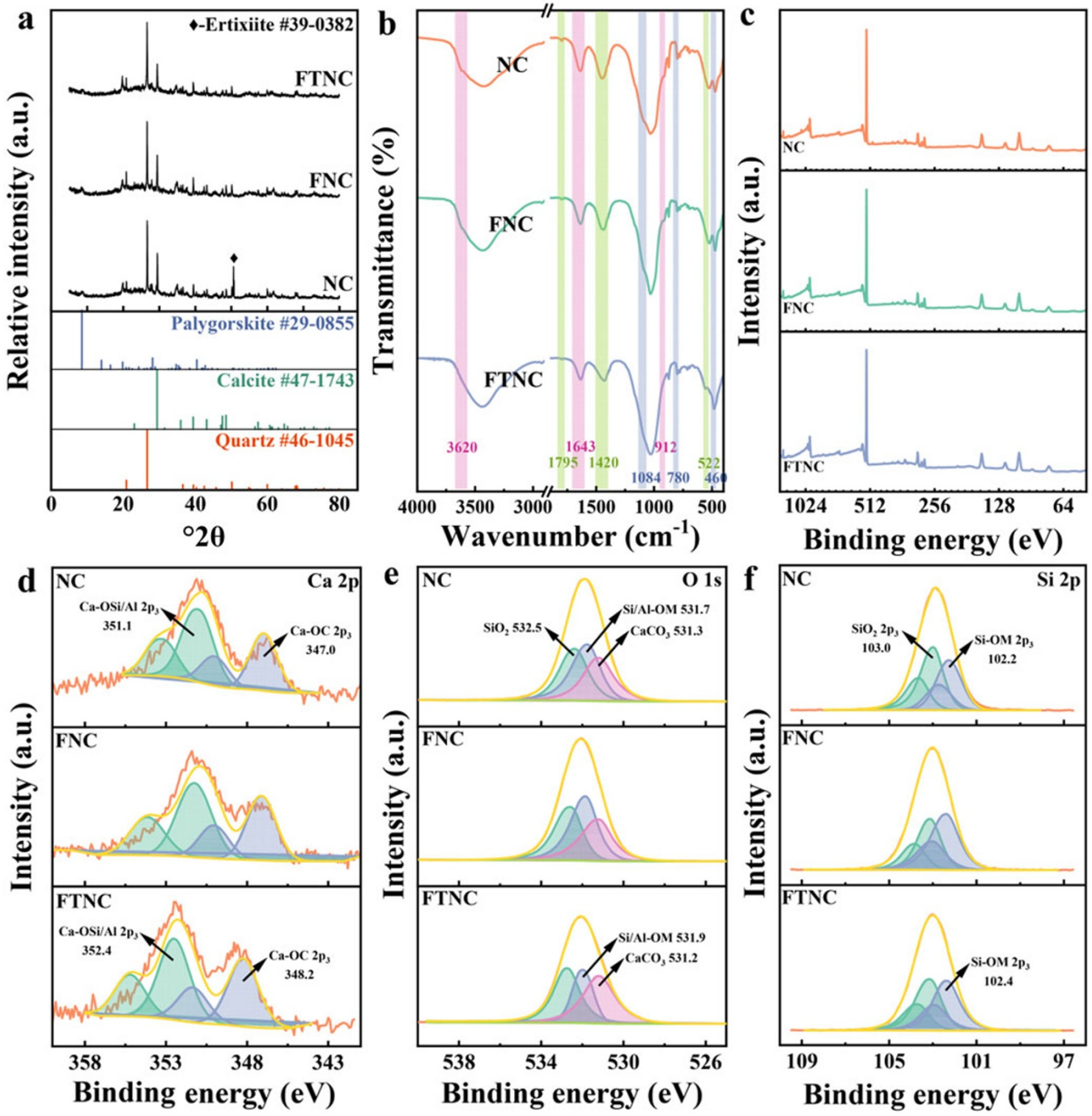


Figure 2. (a) XRD traces, (b) FTIR spectra and (c) XPS survey spectra of NC, FNC and FTNC. Fine XPS spectra of (d) Ca 2p, (e) O 1s and (f) Si 2p for the same samples.

Pore architecture and surface chemical properties

N_2 adsorption–desorption isotherms (Fig. 3c) show that NC exhibits a Type IV isotherm with an H3 hysteresis loop, indicating heterogeneous pore structures (Sing *et al.*, 1985; Kutluay & Ece, 2025). At $P/P_0 \leq 0.40$, the adsorption and desorption branches coincide, indicating monolayer adsorption and the presence of micropores (Storck *et al.*, 1998). When P/P_0 exceeds 0.4, N_2 adsorption increases markedly, attributed to capillary condensation in mesopores and macropores (Bakandritsos *et al.*, 2004), suggesting the presence of slit-like, narrow meso-/macropores within the aggregated silicate particles.

NC has a specific surface area of 64.0 $m^2\ g^{-1}$ and a pore volume of 0.092 mL g^{-1} (Table 1), consistent with severe agglomeration. After mechanical disaggregation (FNC), the specific surface area increases to 87.9 $m^2\ g^{-1}$ (increase of 37%) and the pore volume increases to 0.169 mL g^{-1}. Pore-size distribution (Fig. 3d) shows an increased proportion of pores in the 8–50 nm range, indicating the exposure of previously buried pores. After thermal activation at 600°C (FTNC), the specific surface area (74.8 $m^2\ g^{-1}$) is

https://doi.org/10.1180/clm.2026.10049 Published online by Cambridge University Press

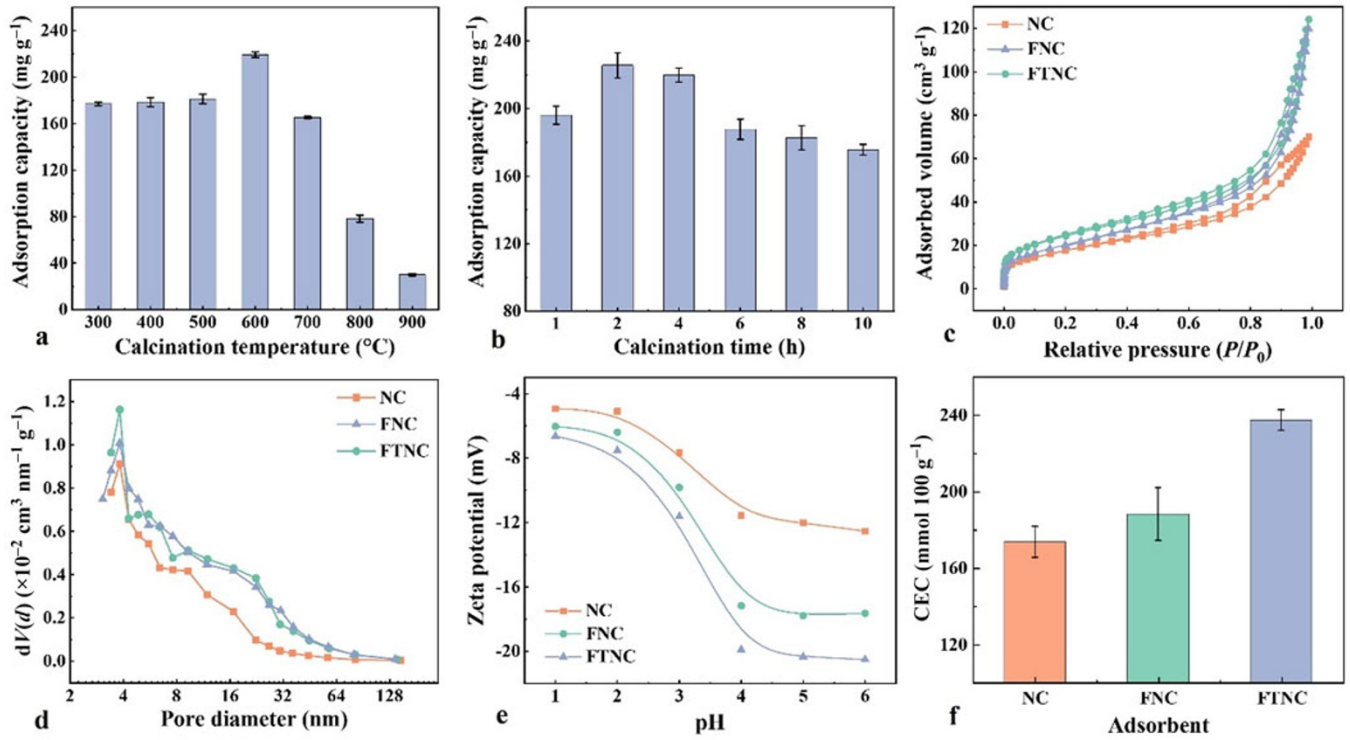


Figure 3. (a,b) Influence of calcination temperature and time on adsorption capacity, (c) N_2 adsorption–desorption isotherm, (d) pore-size distribution curve, (e) zeta potential and (f) CEC values of NC, FNC and FTNC.

Table 1. Specific surface area and pore-structure parameters.

Sample	Specific surface area (m^2 g^{-1})	Pore volume (mL g^{-1})	Pore diameter (nm)
NC	64.0	0.092	3.06
FNC	87.9	0.169	3.81
FTNC	74.8	0.170	3.05

slightly lower than that of FNC (87.9 m^2 g^{-1}), but the pore volume (0.170 mL g^{-1}) remains similar. The pore-size distribution becomes more dispersed (Fig. 3d), with more pores in the 8–50 nm range. The isotherm remains Type IV with an H3 hysteresis loop, indicating that the intrinsic pore structure is not destroyed. Some micropores collapse due to lattice distortion during heating, but pore channel clearance (removal of zeolitic and bound water) compensates for this loss.

Zeta-potential measurements (Fig. 3e) show that at pH 5, FTNC has a zeta potential of –20.4 mV, lower than those of NC (–12.0 mV) and FNC (–17.8 mV). All three samples are negatively charged in the pH range 1–6, enabling electrostatic attraction of Pb^{2+}. The CEC values (mmol 100 g^{-1}) of FNC and NC are negligible compared to that of FTNC (Fig. 3f), indicating that thermal treatment activates previously dormant exchange sites (Nel *et al.*, 2023).

Adsorption behaviour

Effect of initial pH

The effect of initial pH on Pb^{2+} adsorption (200 mg L^{-1} initial concentration of Pb, 25°C, 0.5 g L^{-1} feed ratio) is shown in Fig. 4a. For all three samples, adsorption capacity increases with pH and plateaus at higher pH. The maximum adsorption capacities at pH 5.5 are 153.1 mg g^{-1} (NC), 206.4 mg g^{-1} (FNC) and 237.5 mg g^{-1} (FTNC). At pH 3.0, NC shows no adsorption, whereas FNC and FTNC achieve adsorption capacities of 79.4 and 90.2 mg g^{-1}, respectively, indicating improved pH tolerance after mechanical activation. FTNC maintains effective adsorption even at pH 1–2, demonstrating that thermal treatment activates high-affinity Pb^{2+} binding sites that remain effective at high H^+ concentrations. FTNC reaches adsorption equilibrium at pH 4.0, while NC still shows a 28.6% increase in adsorption capacity from pH 4.0 to 5.5.

Final pH values after adsorption are shown in Fig. 4b & Table S1. At initial pH ≤ 2.0, the final pH is only slightly higher. At initial pH 3.0, the final pH rises to 3.89–4.08. This increase is attributed to carbonate dissolution (consuming H^+) and Pb^{2+} adsorption (reducing free Pb^{2+} and increasing OH^- activity). In the initial pH range 4.0–5.5, the final pH increases only slightly, probably because the acidity is insufficient to disrupt the carbonate structure; the pH change reflects Pb^{2+} adsorption and the release of soluble alkaline species.

Ca release into the supernatant was measured at various initial pH values (Fig. S2). At pH ≤ 2.0, Ca concentration is highest, mainly from acid-induced dissolution of Ca-containing minerals. NC releases more Ca than FNC and FTNC, indicating that soluble Ca salts in NC are removed during washing. FNC and FTNC show similar Ca release at this stage, but only FTNC adsorbs Pb^{2+}, suggesting that adsorption at low pH is not primarily due to Ca ion exchange. At pH 3.0, Ca dissolution decreases, although some Ca is released *via* ion exchange. At pH 4.0–5.5, free Ca increases slightly with pH but remains much lower than at pH ≤ 3.0, indicating that acidity no longer breaks down Ca-containing phases; most of the free Ca comes from ion exchange.

https://doi.org/10.1180/clm.2026.10049 Published online by Cambridge University Press

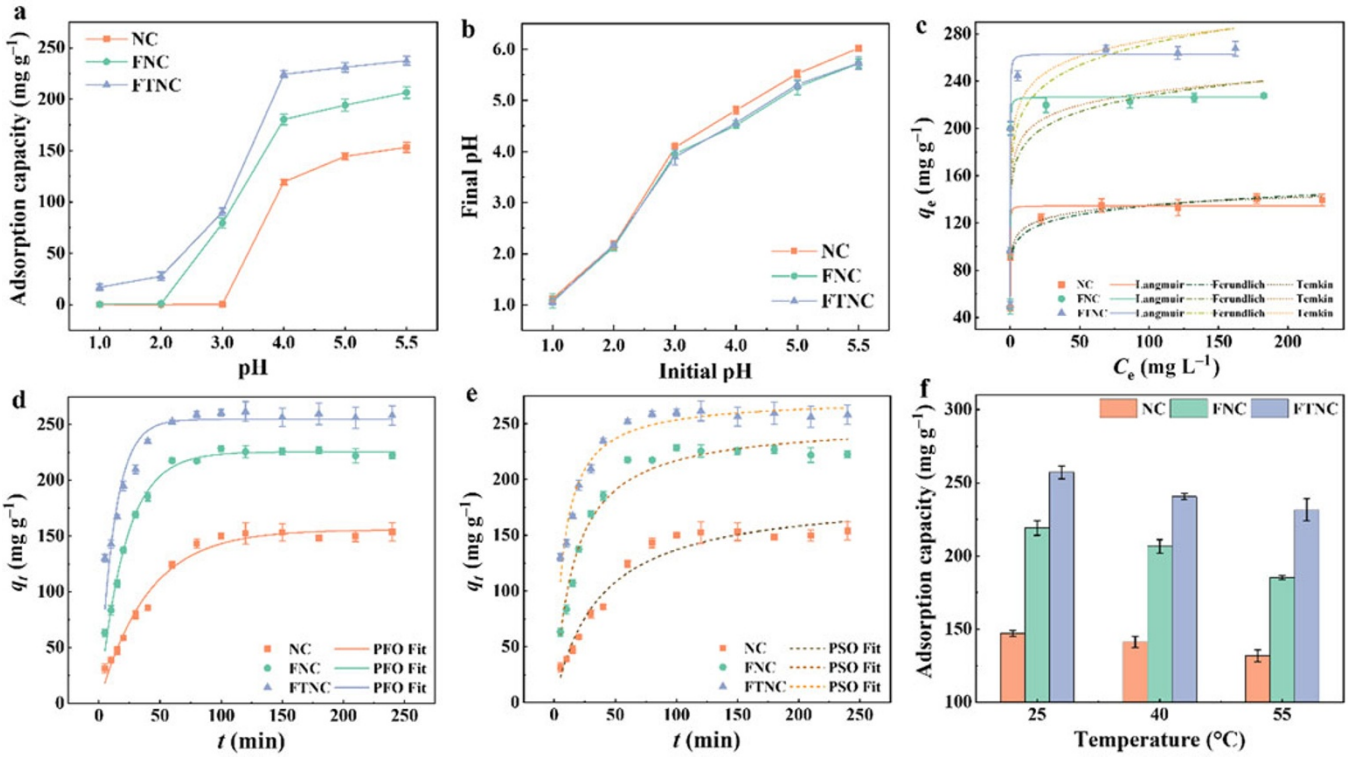


Figure 4. (a) Effect of initial pH on Pb^{2+} adsorption and (b) the corresponding final pH; (c,d) adsorption isotherms and model fits; (e) adsorption kinetics and model fits; and (f) effect of temperature on adsorption. PFO = pseudo-first-order; PSO = pseudo-second-order.

Adsorption isotherms

Adsorption isotherms were obtained at 25°C using Pb^{2+} solutions at pH 5.5 with initial concentrations of 25–300 mg L^{-1} and an adsorbent dosage of 0.5 g L^{-1} (Fig. 4c). Equilibrium adsorption capacities (q_e) are 140.8 mg g^{-1} (NC), 227.9 mg g^{-1} (FNC) and 267.6 mg g^{-1} (FTNC), increasing progressively with activation. The Langmuir model gives the highest R^2 values (0.9718–0.9774) for all samples, indicating monolayer adsorption on uniform active sites. Langmuir maximum capacities (q_m) are 134.5 mg g^{-1} (NC), 226.7 mg g^{-1} (FNC) and 263.2 mg g^{-1} (FTNC), matching the experimental values.

The Langmuir constant K_L decreased with activation: from 25.42 L mg^{-1} (NC) to 22.77 L mg^{-1} (FNC) and further to 19.76 L mg^{-1} (FTNC), indicating that the ions adsorbed on FTNC are mainly in an adsorbed state (Balmer, 2011). The Temkin parameter b, related to adsorption heat, also decreased from 287.29 to 122.80 J mol^{-1} after activation (Table S3), indicating reduced surface energy heterogeneity. Macroscopic adsorption capacity q_m can be viewed as the product of the number of adsorption sites and the probability that those sites are occupied (Ivanović *et al.*, 2025). Although the occupation probability (reflected by K_L) decreases after activation, the total number of accessible sites increases, leading to a net increase in q_m (from 134.5 to 263.2 mg g^{-1}). This suggests that synergistic activation primarily increases site quantity rather than site affinity, shifting the energy distribution from a few high-energy sites to a large number of moderately uniform sites.

Adsorption kinetics

Adsorption kinetics were measured using 200 mg L^{-1} Pb^{2+} at pH 5.5 with 0.5 g L^{-1} adsorbent at 25°C (Fig. 4d,e). All three samples show rapid adsorption within the first 60 min, followed by slower uptake from 60 to 120 min, reaching equilibrium at 120 min. Equilibrium capacities (q_e) are 153.9 mg g^{-1} (NC), 228.4 mg g^{-1} (FNC) and 261.6 mg g^{-1} (FTNC). During the 60–120 min period, NC gains 18.2% of its equilibrium capacity, whereas FNC and FTNC gain only 3.5% and 3.6%, respectively, indicating that activated samples approach equilibrium much earlier. Kinetic parameters (Table S4) show that the pseudo-first-order model yields R^2 values of 0.9796–0.9899, while the pseudo-second-order model yields values of 0.9514–0.9674. Both models fit the data reasonably well, reflecting the complexity of solid–liquid adsorption. As noted by Vareda (2023), when both adsorbate and active sites are limited, the kinetics may exhibit pseudo-second-order characteristics. However, relying solely on R^2 to distinguish between kinetic models is insufficient, because diffusion and other non-ideal processes also influence the overall rate (Simonin, 2016). The rate constant k_1 increases from 0.0252 min^{-1} (NC) to 0.0468 min^{-1} (FNC) and 0.0805 min^{-1} (FTNC), confirming that activation increases mass transfer efficiency by exposing more active sites and shortening diffusion pathways.

Adsorption thermodynamics

Adsorption thermodynamic experiments were conducted at 298.15, 313.15 and 328.15 K (Fig. 4f & Table S5). As temperature increased from 25°C to 55°C, equilibrium adsorption capacity (q_e) decreased: from 146.95 to 131.64 mg g^{-1} for NC, from 219.16 to 185.22 mg g^{-1} for FNC and from 257.11 to 231.45 mg g^{-1} for FTNC, indicating an exothermic adsorption process. Thermodynamic parameters derived from $\ln(q_e/C_e)$ *vs* $1/T$ plots (Fig. S5) confirm exothermicity, with negative ΔH values ranging from −4.72 to −8.58 kJ mol^{-1}, following the order FTNC

https://doi.org/10.1180/clm.2026.10049 Published online by Cambridge University Press

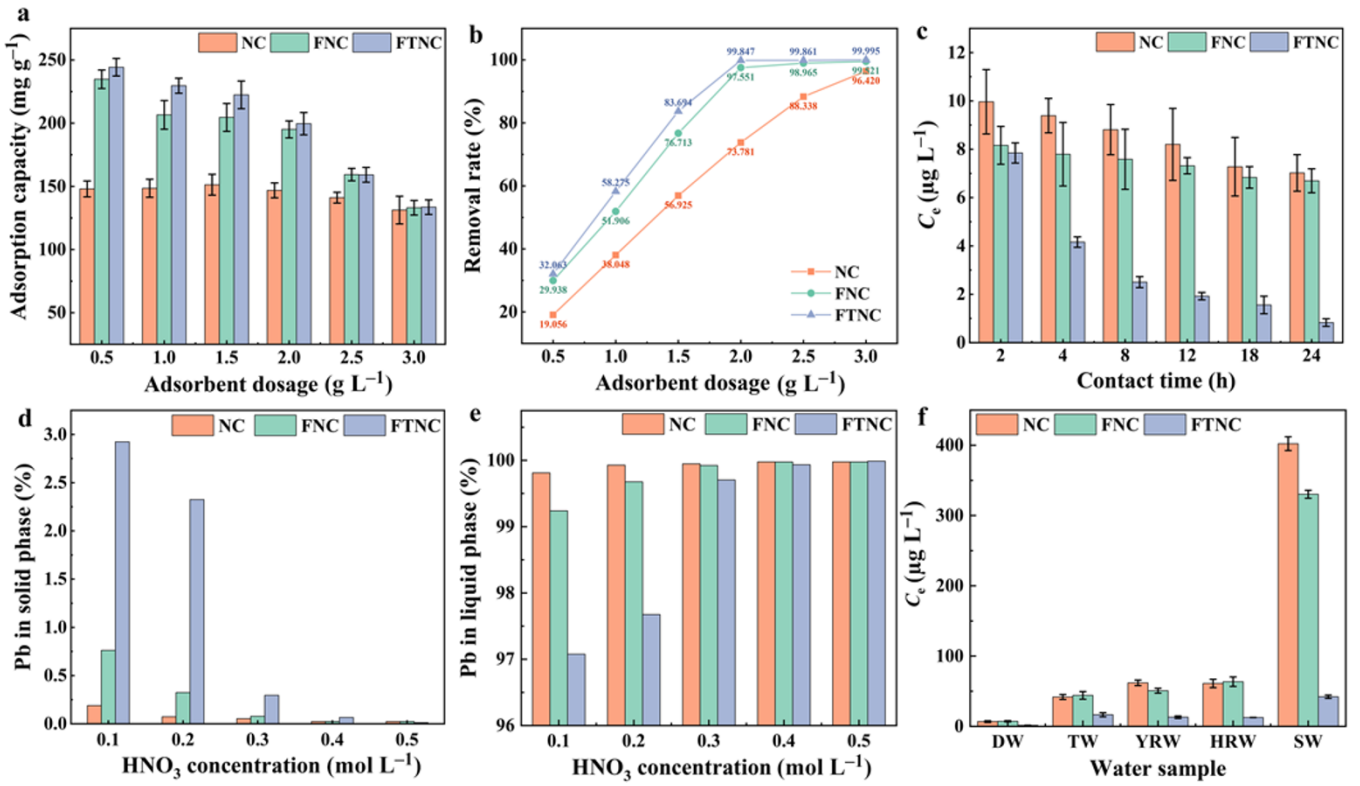


Figure 5. (a) Effect of adsorbent dosage on adsorption capacity; (b) effect of adsorbent dosage on removal efficiency; (c) residual Pb^{2+} concentration over time at low initial concentration; (d) residual Pb^{2+} on adsorbent after elution with various HNO_3 concentrations; (e) Pb recovery rate in leachate after elution with various HNO_3 concentrations; and (f) residual Pb^{2+} concentration in real water samples after adsorption.

> FNC > NC. Negative ΔS values (−14.29 to −21.25 J (mol K^{-1})$^{-1}$) suggest reduced randomness at the solid–liquid interface, implying ordered arrangement of adsorbed ions. Negative ΔG values at all temperatures confirm spontaneity; $|\Delta G|$ decreases with rising temperature, reflecting diminished spontaneity at higher temperatures. The $|\Delta G|$ values for FTNC (3.28–2.81 kJ mol^{-1}) are consistently larger than those for FNC (2.25–1.61 kJ mol^{-1}) and NC (0.46–0.03 kJ mol^{-1}), indicating a stronger thermodynamic driving force for Pb^{2+} adsorption after activation. The ΔG values fall within −20 to 0 kJ mol^{-1}, suggesting that adsorption is primarily governed by physisorption or weak chemical interactions, with lower temperatures being thermodynamically favourable for Pb^{2+} removal.

Deep purification capability

The removal performance of the adsorbents was evaluated at pH 5.5 and 25°C under high-concentration (400 mg L^{-1}) and low-concentration (1000 μg L^{-1}) Pb^{2+} conditions. For high-concentration Pb^{2+}, adsorbent dosage was varied from 0.5 to 3.0 g L^{-1} (Fig. 5a,b). At 3.0 g L^{-1}, removal efficiencies reach 96.42% (NC), 99.52% (FNC) and >99.99% (FTNC). FTNC achieves 99.85% removal at the lower dosage of 2.0 g L^{-1}, indicating that activation improves the utilization efficiency of active sites. This enhancement results from mechanical disaggregation (exposing buried surfaces) and thermal activation (increasing accessible binding site density).

For the low-concentration Pb^{2+} solution (1000 μg L^{-1}) with an adsorbent dosage of 1.0 g L^{-1} (Fig. 5c), all three materials reduced the Pb^{2+} concentration to below the World Health Organization (WHO) drinking water guideline of 10 μg L^{-1} within 2 h, confirming their baseline capability for deep purification. After 24 h, however, the residual Pb^{2+} concentration with FTNC was 0.83 μg L^{-1}, markedly lower than those with NC (7.02 μg L^{-1}) and FNC (6.69 μg L^{-1}). This difference points to a key mechanistic distinction: while both FNC and FTNC possess sufficient active sites for rapid initial uptake, FTNC's thermally activated structure appears to offer not only more sites but also stronger binding affinity for trace-level Pb^{2+}, allowing effective capture even under an extremely low concentration gradient. By contrast, the slower kinetics and weaker binding of NC and FNC prevent them from driving the concentrations down to sub-μg L^{-1} levels within the same timeframe.

Elution of Pb^{2+} and purification of contaminated water samples

Elution of the adsorbed Pb^{2+} was tested using dilute HNO_3 (0.1–0.5 mol L^{-1}; Fig. 5d,e). At 0.5 mol L^{-1} HNO_3, Pb^{2+} was almost completely transferred to the liquid phase, indicating reversible adsorption under acidic conditions. The optimal elution conditions were therefore set as: 0.5 mol L^{-1} HNO_3, solid-to-liquid ratio of 2.0 g L^{-1} and stirring at 25°C for 2 h.

Evaluating adsorbent performance in DW alone is insufficient because real water matrices are far more complex. Even artificially prepared simulated surface water cannot fully capture the complexity of natural organic and inorganic components. Simply adding inorganic cations and anions does not reflect real-world conditions (Akhter *et al.*, 2023). We therefore collected actual water samples from multiple sources: the Yangtze River (YRW, Nanjing, Jiangsu, China), the Yellow River (HRW, Baotou,

https://doi.org/10.1180/clm.2026.10049 Published online by Cambridge University Press

Inner Mongolia, China) and seawater (SW, Tianjin, China). DW (Milli-Q® Integral 10 laboratory pure water system) and TW (Hohhot, Inner Mongolia, China) were also used. A small volume of concentrated Pb^{2+} solution was spiked into each water sample to reach a nominal Pb^{2+} concentration of ~1000 μg L^{-1}. After thorough mixing, the samples were filtered through a 0.45 μm membrane to obtain the artificially contaminated water samples. Figure 5f shows the purification results for low-concentration Pb^{2+} in these water matrices using the three adsorbents. All three materials reduced Pb^{2+} to varying extents, even under complex conditions. For freshwater samples, the Pb^{2+} concentration in the supernatant dropped from 1000 μg L^{-1} to below 80 μg L^{-1}. In the high-salinity seawater samples, NC and FNC achieved 60–70% removal. Notably, FTNC reduced the Pb^{2+} concentration in seawater from 1000 μg L^{-1} to below 50 μg L^{-1}. This excellent anti-interference performance opens up multiple possibilities for practical applications.

Synergistic adsorption mechanism of multi-mineral intergrowth

The Pb^{2+}-saturated samples were characterized to understand how activation increases adsorption on NC, FNC and FTNC.

Phase analysis of Pb-saturated samples

XRD traces of Pb-saturated samples (NC-Pb, FNC-Pb, FTNC-Pb; Fig. 6a) show diffraction peaks assigned to $PbCO_3$ (JCPDS No. 47-1734), $PbSiO_3$ (JCPDS No. 29-0782) and PbO (JCPDS No. 38-1477). $PbCO_3$ dominates, suggesting that carbonate minerals are the main sink for Pb^{2+} fixation. This agrees with the sharp decrease in adsorption capacity above 800°C (Fig. 3a), where calcite decomposes. The presence of $PbSiO_3$ indicates another immobilization route: ion exchange, whereby Pb^{2+} replaces structural cations (e.g. Na^+, Mg^{2+}) on silicate surfaces. All three samples contain both $PbCO_3$ and $PbSiO_3$, pointing to a dual mechanism: carbonate-dominated precipitation/complexation together with silicate-mediated ion exchange. The weak PbO signals and the elevated pH of Pb-saturated samples suggest that the alkalinity of adsorbents promotes some Pb^{2+} precipitation, although this is a minor pathway.

Chemical state analysis of Pb-saturated samples

XPS survey spectra (Fig. S1b) show Pb 4d (412.0–434.3 eV) and 4f (136.9–141.8 eV) signals in the Pb-saturated samples. The Pb 4f core-level spectra (Fig. 6b) show three chemical states – PbO (137.6 eV), $PbCO_3$ (138.3 eV) and $PbSiO_3$ (138.7 eV) – matching the XRD findings. Their relative intensities reveal how the mechanism changes with activation. The PbO signal is lower in FNC-Pb and FTNC-Pb than in NC-Pb, meaning that activation reduces surface alkalinity and thus suppresses precipitation as a removal pathway. The $PbSiO_3$ signal is higher in FTNC-Pb, indicating that thermal activation makes more $Si–O^-$ active sites available, which promotes ion exchange-mediated Pb binding. The $PbCO_3$ signal remains unchanged, showing that carbonate mineralization survives activation. This is noteworthy because calcite normally decomposes at high temperatures.

In the O 1s spectra (Fig. 6c), a new Pb–O peak appears at 530.8 eV after adsorption. Compared with the pristine samples (Fig. 2), the $CaCO_3$ and Al–O–Al/Si–O peaks shift by 0.1 and 0.3 eV, respectively, while the SiO_2 peak does not change. Ca 2p core-level spectra (Fig. 2d) show that after saturation adsorption, the binding energy of the Ca–O–C environment is 348.8 eV, close to the 348.2 eV observed for FTNC before adsorption. This suggests that activation shifts the binding energy in a direction favouring ion exchange. Moreover, samples with higher saturation adsorption capacities exhibit lower Ca–O–C binding energies, implying greater involvement of Ca in the adsorption process. C 1s spectra (Fig. 6e) corroborate this: the carbonate peak shifts from 289.4 to 289.2 eV. The Si–O–*M* peak (Fig. 6f) shifts by 0.1 eV. Both shifts confirm that Pb^{2+} interacts with carbonate and silicate components.

Together, the XPS data show a clear division of labour: carbonates act as the primary, stable sink for Pb^{2+} (unchanged $PbCO_3$ signals), while silicate sites contribute *via* ion exchange – a role that increases with thermal activation (higher $PbSiO_3$ in FTNC-Pb). In activated samples, less PbO forms, indicating a shift from non-specific precipitation to more targeted chemical binding. This is favourable for long-term immobilization.

Quantitative evidence of ion exchange

XRF analysis (Table S1) shows a marked decrease in Si content after washing, stirring and sieving, attributed to the removal of inert quartz particles that do not contribute to adsorption. To quantify the contribution of cation exchange, we performed the following experiments. First, 1.0 g of adsorbent was added to 1000 mL of DW (pH 5.5) containing Pb^{2+}, with continuous stirring. The DW contained no detectable metal cations before this addition. Over time, the adsorbed Pb amount gradually increased. At regular intervals, a small suspension aliquot was sampled for ICP-OES analysis. The mass loss of adsorbent and volume change of the solution were negligible. The concentrations of Na^+, K^+, Mg^{2+} and Ca^{2+} in the supernatant were measured as a function of adsorbed Pb^{2+}. A control experiment was performed under identical conditions but without Pb^{2+}. In the main experiment, the released cations came from both Pb^{2+} exchange and adsorbent dissolution. In the control, only dissolution contributed. Subtracting the control values from the main experiment gave the net cations released solely by ion exchange.

Using the solid-to-liquid ratio, we then calculated (in mmol) both the amounts of the four cations involved in exchange and the amount of Pb fixed to the adsorbent. For charge equivalence, divalent cation amounts were divided by 2. The normalized results are shown in Fig. 6g. Ca release correlates positively with Pb^{2+} uptake, and the amount of Ca^{2+} released is much higher than those of Na^+, K^+ or Mg^{2+}. Thus, Ca^{2+} dominates the ion-exchange process, consistent with the predominance of $PbCO_3$ seen in XRD and XPS. Compared with NC, the Ca concentrations for FNC and FTNC increased only slightly, and the slopes of their correlation lines changed little. This suggests that thermal activation does not impair Ca-mediated ion exchange (Fig. 6g). Mg^{2+} also participates in exchange, although to a lesser extent than Ca. Activation gradually increases the exchange activity of Mg^{2+}: the amount of Mg released increases, and the fitting slope becomes steeper. The increase from NC to FNC probably reflects the removal of inert particles, disruption of soft agglomerates and increased specific surface area, which expose more Mg active sites. The further increase from FNC to FTNC suggests that thermal treatment activates previously inactive sites, possibly by removing water from mineral crystal pores and allowing Pb^{2+} to enter (Fig. 6g). The trend is even more pronounced for Na^+ and K^+. For untreated adsorbents, the fitted slope is near zero, indicating negligible Na/K involvement in exchange. After thermal activation, both cations become significantly engaged: their supernatant concentrations now correlate with Pb^{2+} uptake (the slope increases). The underlying mechanism may be similar to that proposed for Mg^{2+}.

https://doi.org/10.1180/clm.2026.10049 Published online by Cambridge University Press

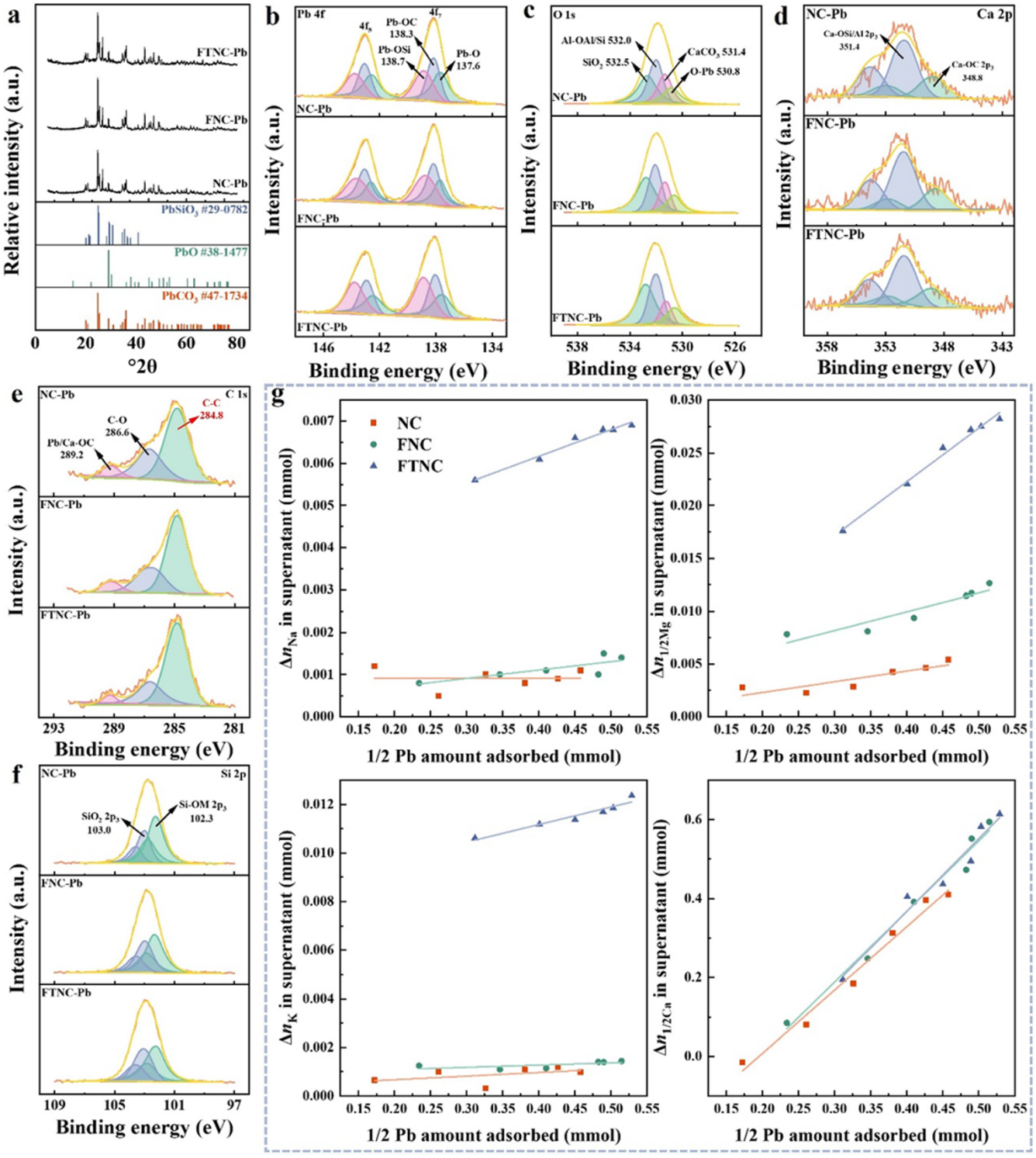


Figure 6. (a) XRD traces and (b–f) high-resolution XPS spectra of saturated adsorbent samples: (b) Pb 4f, (c) O 1s, (d) Ca 2p, (e) C 1s and (f) Si 2p. (g) Amounts of Na^{+}, K^{+}, Mg^{2+} and Ca^{2+} released into the supernatant during Pb2+ adsorption.

To quantitatively assess the contribution of total cation exchange ($Na^{+} + K^{+} + Mg^{2+} + Ca^{2+}$) to Pb^{2+} adsorption, we normalized all amounts to charge equivalents (mmol of +1 charge). From the fitted linear equations, we obtained the charge-equivalent adsorbed Pb and the corresponding charge-equivalent released cations. Table S6 summarizes these values.

The total exchanged cations account for at least 72.6% of the adsorbed Pb^{2+} (on a charge-equivalent basis). This indicates that ion exchange is the dominant adsorption mechanism. Moreover, activation increases the total amount of cations released during adsorption. Together, the ion-exchange data show a clear hierarchy linked to the structural roles of the cations. Ca^{2+}

https://doi.org/10.1180/clm.2026.10049 Published online by Cambridge University Press

(carbonate-associated, readily exchangeable) dominates. Mg^{2+} (silicate-bound, moderately accessible) follows. Na^{+} and K^{+} (located in interlayers or channels) require thermal activation to become exchangeable. Activation thus progressively releases these sites, increasing Pb^{2+} adsorption.

Contribution of electrostatic attraction

Zeta-potential measurements (Fig. 3c) show that NC, FNC and FTNC all carry negative surface charges at pH 1–6, which can attract positively charged Pb^{2+}. The negative charge increases with pH and levels off above pH 4. At pH ≥ 5, the zeta potentials are approximately –12.0 mV (NC), –17.8 mV (FNC) and –20.4 mV (FTNC).

Surface negativity increases with activation in the order NC < FNC < FTNC. Two factors explain this trend. First, mechanical disaggregation exposes negatively charged surfaces that were previously buried. Second, thermal activation probably increases the density of deprotonated Si–O^{-} sites. This stronger negative charge then promotes electrostatic capture of Pb^{2+}.

The zeta-potential trend follows the adsorption capacity order (NC < FNC < FTNC). However, the surface-charge difference between NC and FTNC is only ∼8.4 mV, whereas the adsorption capacity increases by >120 mg g^{-1}. This disparity indicates that electrostatic attraction alone cannot explain the full increase. Rather, activation mainly increases the density of active sites and promotes specific chemical binding (ion exchange and carbonate mineralization), with electrostatic attraction playing a complementary role.

Synergistic adsorption mechanism model

From the results presented earlier, we propose a synergistic adsorption mechanism for the multi-mineral intergrowth, involving four pathways: (1) calcite-dominated ion exchange (primary): $CaCO_3 + Pb^{2+} \rightarrow PbCO_3 + Ca^{2+}$; (2) silicate cation exchange (supplementary): ≡Si–O–M + Pb^{2+} → ≡Si–O–Pb + M (M = Na^{+}, K^{+}, Mg^{2+}, Ca^{2+}); (3) electrostatic attraction: negatively charged surfaces interact with Pb^{2+}; and (4) *in situ* precipitation: local pH increase leads to $PbO/Pb(OH)_2$ formation.

The contribution of each pathway changes with activation. Calcite-dominated exchange remains primary in all samples, as evidenced by the dominant $PbCO_3$ in the XRD/XPS results and the strong Ca^{2+} release in the ICP-OES results. Silicate exchange, already present in pristine NC, becomes significantly greater after thermal activation – particularly for Na^{+} and K^{+}, which are only mobilized upon heating. Natural minerals contain abundant bound water in their lattices; heat treatment can cause dehydroxylation. Previous work has shown that dehydroxylation of clay minerals promotes heavy metal adsorption from water (Chen *et al.*, 2017; Ondruška *et al.*, 2017; Cheng *et al.*, 2019; Wu *et al.*, 2025; He *et al.*, 2026), mainly by increasing the contact probability between adsorbate and active sites. Electrostatic attraction follows the order of surface negativity: FTNC > FNC > NC. Precipitation plays only a minor role, consistent with the weak PbO signals and their suppression in activated samples.

Our multi-scale engineering approach – compositional optimization, aggregate disintegration, structural activation and surface modification – systematically facilitates these mechanisms. Mechanical disaggregation removes inert quartz and exposes buried active surfaces, increasing the availability of both carbonate and silicate exchange sites. Thermal activation achieves a critical synergy: it preserves carbonate activity while activating silicate exchange sites and increasing surface negative charge. As a result, the primary and supplementary mechanisms work together rather than competing.

FTNC thus functions as a multi-pathway synergistic adsorption system, offering superior adsorption capacity, profound purification ability and acid tolerance relative to the pristine material.

Conclusions

A low-grade, natural, mixed attapulgite clay intergrowth (NC) with large reserves in nature was activated using reagent-free physical treatments (mechanical disaggregation followed by thermal activation) to obtain two clay-derived adsorbents: FNC and FTNC. The maximum Pb^{2+} adsorption capacities of NC, FNC and FTNC were 153.1, 206.4 and 237.5 mg g^{-1}, respectively, with corresponding removal efficiencies of 96.42%, 99.52% and 99.99%. The adsorption follows the Langmuir isotherm and pseudo-first-order kinetics, indicating a spontaneous exothermic process. The adsorbed Pb^{2+} can be efficiently eluted with dilute acid. Characterization shows that NC is a mixed intergrowth primarily composed of quartz, calcite and attapulgite. Mechanical activation removes soluble salts and inert impurities, disrupts soft agglomerates and improves dispersion. Subsequent thermal activation at 600°C preserved the mineral phases but removes channel water, thereby facilitating ion diffusion. The adsorption involves three synergistic mechanisms: (1) ion exchange with carbonate and silicate minerals, forming $PbCO_3$ and $PbSiO_3$ (with calcite as the dominant contributor); (2) *in situ* precipitation of PbO induced by the alkalinity of intergrowth; and (3) electrostatic attraction between negatively charged surfaces and Pb^{2+}. Mechanical activation improves performance by removing inactive components and improving dispersion. Thermal activation further increases adsorption capacity by activating silicate exchange sites and preserving carbonate activity, allowing effective Pb^{2+} adsorption even at pH 1.

Supplementary material. The supplementary material for this article can be found at https://doi.org/10.1180/clm.2026.10049.

CRediT authorship contribution statement. Huan Zhang: Investigation, Formal analysis, Data curation, Writing – original draft. Hang Lu, Zhihui Mao: Writing – review & editing, Formal analysis, Software. Zongyang Liu, Siyuan Wang: Formal analysis, Software. Wenbo Wang: Conceptualization, Writing – review & editing, Resources, Methodology, Supervision.

Financial support. This research was supported by the following projects: the National Natural Science Foundation of China (22468033); the Key R&D and Achievement Transformation Project of Inner Mongolia Autonomous Region (2023YFHH0057); the Natural Science Foundation of Inner Mongolia Autonomous Region (2024SHZR1554); the Jiangsu Provincial Key Laboratory of Palygorskite Science and Applied Technology, Huaiyin Institute of Technology (HPK202302); and the Program of Higher-Level Talents of Inner Mongolia University (10000-23112101/017).

Competing interests. The authors declare that they have no known competing financial interests or personal relationships that could have appeared to influence the work reported in this paper.

References

Abdel-Azim S.M., Aboul-Gheit N.A.K., Younis S.A. & Ahmed S.M. (2025) Synergistic role of pillared bentonite with single and binary Fe/Al-polyoxocations on Pb^{2+} adsorption recovery from hard water under competitive and non-competitive effects. *Applied Clay Science*, **267**, 107716.

Abujayyab M., Hasan S.W., Arafat H.A. & Banat F. (2025) High-efficiency lithium recovery from desalination brine *via* Mn–Al layered double hydroxide. *Desalination*, **616**, 119376.

Akhter F., Soni H.L., Jamali A.R., Zoppas F.M. & Ibrahim S.M. (2023) Efficient adsorption of lead(II) ions from artificial wastewater by organically tailored *vs* TEOS-doped silica aerogels: synthesis, characterization and isotherm studies. *Water, Air, & Soil Pollution*, **234**, 180.

Ali A.B., Al-Meer S., Nasser M.S. & Hussein I.A. (2025) Microwave-synthesized composite preformed particle gels based on tragacanth gum and palygorskite for high-salinity high-temperature conditions. *Applied Clay Science*, **278**, 108006.

Amor A.A., Messaitfa A., Tabchouche A., Abdeslam S.B., Zighmi S., Amor F.Z.A. & Omar A.A. (2025) Biosorption of fluoride ions from drinking water at southern Algeria using the eggshell waste beads in an up flow packed bed column: a chemical study and solution modeling. *Desalination*, **600**, 118521.

Bakandritsos A., Steriotis T. & Petridis D. (2004) High surface area montmorillonite–carbon composites and derived carbons. *Chemistry of Materials*, **16**, 1551–1559.

Balmer R.T. (2011) Introduction to statistical thermodynamics. Pp. 727–762. in: *Modern Engineering Thermodynamics*. Academic Press, Boston, MA, USA.

Bao T., Damtie M.M., Wang C.Y., Chen Z.J., Tao Q., Wei W. *et al.* (2024) Comprehensive review of modified clay minerals for phosphate management and future prospects. *Journal of Cleaner Production*, **447**, 141425.

Boudriche L., Calvet R., Hamdi B. & Balard H. (2012) Surface properties evolution of attapulgite by IGC analysis as a function of thermal treatment. *Colloids and Surfaces A: Physicochemical and Engineering Aspects*, **399**, 1–10.

Chen H., Jin Y.X., Wu J.Y. & Yan H. (2025) Significantly improving the colloidal stability of selenium disulfide in water and antifungal activity by using palygorskite clay. *Applied Clay Science*, **265**, 107659.

Chen Q., Gray M.R. & Liu Q. (2017) Irreversible adsorption of asphaltenes on kaolinite: influence of dehydroxylation. *Energy & Fuels*, **31**, 9328–9336.

Cheng Y., Xing J., Bu C., Zhang J., Piao G., Huang Y. *et al.* (2019) Dehydroxylation and structural distortion of kaolinite as a high-temperature sorbent in the furnace. *Minerals*, **9**, 587.

Cui Y.T., Zhou Y., Cheng M.Q., Fang W., Wang Y.L., Chen C. *et al.* (2025) Synergistic valorization of red mud and spent coffee grounds *via* one-step hydrothermal carbonization for high-efficiency Pb^{2+} and Cd(II) removal from wastewater. *Desalination*, **616**, 119349.

Diop M.B., Molez L., Bouguerra A., Diouf A.N. & Grutzeck M.W. (2014) Manufacturing brick from attapulgite clay at low temperature by geopolymerization. *Arabian Journal for Science and Engineering*, **39**, 4351–4361.

Fan J.H., Liu X.J., Yang M.Y., Liu M.Y., Ma Q.C., Fu L.J. *et al.* (2025) Synthesis of zeolite 4A from low-grade kaolin containing muscovite and quartz *via* ultrafast Joule heating route: a comparison with conventional calcination. *Applied Clay Science*, **275**, 107889.

Han L., Wang Y.W., Zhao W.T., Zhang H., Guo F., Wang T.Y. & Wang W.B. (2022) Cost-effective and eco-friendly superadsorbent derived from natural calcium-rich clay for ultra-efficient phosphate removal in diverse waters. *Separation and Purification Technology*, **297**, 121516.

He M.Y., Zhu Y., Yang Y., Han B.P. & Zhang Y.M. (2011) Adsorption of cobalt(II) ions from aqueous solutions by palygorskite. *Applied Clay Science*, **54**, 292–296.

He X., Wang C., Hu H., Huang J. & Jiang T. (2026). Revealing the immobilization mechanism of radioactive Cs^{+} through tailored mineral lattice architectures: inspiration from natural mineral structures. *Journal of Environmental Chemical Engineering*, **14**, 120951.

Hu C., Teng F.Y., Yin X.J., Wang P., He B.Y. & Zhu L. (2025) Adsorption of heavy metals using cysteine-modified pillared montmorillonite: mechanisms and characteristics. *Applied Clay Science*, **276**, 107923.

Huang X.J., Zhu W.X., Yang R., Meng D., Zhang X.Y., Wang Z.L. & Hu W.J. (2026) Mechanical activation induces attapulgite microstructure to boost Pb^{2+} and Cd(II) adsorption. *Separation and Purification Technology*, **382**, 135822.

Ivanović T., Tomović T., Popović D., Miladinović J., Arrad M., & Miladinović Z. (2025). A simplified method for enhanced accuracy in calculating adsorption thermodynamic parameters. *The Journal of Chemical Thermodynamics*, **208**, 107517.

Kadir S., Erkoyun H., Külah T., Eren M., Helvacı C. & Demiral B. (2025) Occurrence and genesis of hectorite and mixed-layer-illite/hectorite in argillaceous sediments interlayered with Neogene borate deposits, Emet, Türkiye. *Applied Clay Science*, **267**, 107737.

Kutluay S. & Ece M.Ş. (2025) Exploring enhanced gas-phase toluene adsorption by engineered a novel magnetic nanoadsorbent modified with p-aminobenzoic acid: insights on characterization, performance, kinetics, isotherm, mechanism and reusability. *Separation and Purification Technology*, **359**, 130874.

Langmuir I. (1918) The adsorption of gases on plane surfaces of glass, mica and platinum. *Journal of the American Chemical Society*, **40**, 1361–1403.

Liu Z.Y., Zhang H., Mao Z.H., Shan Z.Y., Wang S.Y., Wang S.L. *et al.* (2026) Asymmetric B–O–Ca coordination in a $Ca_2B_2O_5$/silicate heterostructure enables efficient heavy metal capture across trace to high concentrations. *Desalination*, **628**, 120077.

Lu Y.S. & Wang A.Q. (2022) From structure evolution of palygorskite to functional material: a review. *Microporous and Mesoporous Materials*, **333**, 111765.

Lu Y.S., Mu B., Kang Y.R., Gao W.T. & Wang A.Q. (2025) Enhanced dispersion of mixed-dimensional palygorskite clay *via* high-pressure homogenization and its synergistic reinforcement in chitosan composites. *Applied Clay Science*, **270**, 108000.

Luo J.Z., Cai Y.Y., Yu J., Huang J.F. & Yan J.H. (2025) Phosphate-modified biochar-mineral-based composites for heavy metal removal in acidic environments: development and efficiency. *Applied Clay Science*, **276**, 107924.

Nel T., Bruneel Y. & Smolders E. (2023) Comparison of five methods to determine the cation exchange capacity of soil. *Journal of Plant Nutrition and Soil Science*, **186**, 311–320.

Ondruška J., Štubňa I., Trnovcová V., Vozár L. & Bačík P. (2017). Polarization currents in illite at various temperatures. *Applied Clay Science*, **135**, 414–417.

Peng H.N., Chen P., Wu Y.Q., Chen C.H. & Wang D.M. (2025) Synergistic preparation of organic solvent nanofiltration membranes from polydopamine/polyethyleneimine interlayers with aminated attapulgite. *Separation and Purification Technology*, **355**, 129503.

Seyama H. & Soma M. (1984) X-ray photoelectron spectroscopic study of montmorillonite containing exchangeable divalent cations. *Journal of the Chemical Society, Faraday Transactions 1*, **80**, 237–248.

Shi T., Liu Y.M., Zhang Y.L., Lan Y.J., Zhao Q.F., Zhao Y.J. & Wang H.B. (2022) Calcined attapulgite clay as supplementary cementing material: thermal treatment, hydration activity and mechanical properties. *International Journal of Concrete Structures and Materials*, **16**, 10.

Simonin J.P. (2016). On the comparison of pseudo-first order and pseudo-second order rate laws in the modeling of adsorption kinetics. *Chemical Engineering Journal*, **300**, 254–263.

Sing K.S.W., Everett D.H., Haul R.A.W., Moscou L., Pierotti R.A., Rouquerol J. & Siemieniewska T. (1985) Physical and biophysical chemistry division commission on colloid and surface chemistry including catalysis. *Pure and Applied Chemistry*, **57**, 603–619.

Sosulnikov M.I. & Teterin Y.A. (1991) XPS study of calcium, strontium, barium and their oxides. *Doklady Akademii Nauk SSSR*, **317**, 418–421.

Storck S., Bretinger H. & Maier W.F. (1998) Characterization of micro- and mesoporous solids by physisorption methods and pore-size analysis. *Applied Catalysis A: General*, **174**, 137–146.

Su P.D., Wang Q.Q., Zhang C.H., Li Y.X., Jiao L.J., Su M. *et al.* (2025) A critical review of amyloid fibrils composites as emerging materials for the removal of metal ions from water: synthesis, characteristics, removal performance and mechanism. *Desalination*, **615**, 119243.

Sun P., Zhang W., Zou B.Z., Wang X.Y., Zhou L.C., Ye Z.F. & Zhao Q.L. (2021) Efficient adsorption of Cu(II), Pb^{2+} and Ni(II) from waste water by PANI@APTS–magnetic attapulgite composites. *Applied Clay Science*, **209**, 106151.

Tang L., Zhang P. & Lang C.Y. (2025) Synthesis, characterization and study of Sb(III) adsorption from aqueous solution by iron–aluminum pillared attapulgite. *Journal of Solid State Chemistry*, **341**, 125085.

Temkin M.J. & Pyzhev V. (1940) Recent modifications to Langmuir isotherms. *Acta Physiochim URSS*, **12**, 217–225.

Teng C., Zhang K., Guo J., Li T. & Xu Y. (2025) Construction of two-dimensional zeolitic–imidazolate frameworks for enhanced Pb^{2+} and Cd(II) removal in industrial wastewater. *Desalination*, **615**, 119254.

https://doi.org/10.1180/clm.2026.10049 Published online by Cambridge University Press

Vareda J.P. (2023) On validity, physical meaning, mechanism insights and regression of adsorption kinetic models. *Journal of Molecular Liquids*, **376**, 121416.

Wang S.J., Liu X.X., Zhang C.Y., Hu W.J., Liu Y.C., Fu X.Z. *et al.* (2025a) Adsorption and selective mechanism of Pb^{2+} and Cd^{2+} on the surface of calcined modified attapulgite. *Separation and Purification Technology*, **353**, 128377.

Wang W.B. & Wang A.Q. (2016) Recent progress in dispersion of palygorskite crystal bundles for nanocomposites. *Applied Clay Science*, **119**, 18–30.

Wang W.B., Tian G.Y., Zhang Z.F. & Wang A.Q. (2016) From naturally low-grade palygorskite to hybrid silicate adsorbent for efficient capture of Cu(II) ions. *Applied Clay Science*, **132–133**, 438–448.

Wang W.B., Zhao W.T., Zhang H., Xu J., Zong L., Kang Y.R. & Wang A.Q. (2021) Mesoporous polymetallic silicate derived from naturally abundant mixed clay: a potential robust adsorbent for removal of cationic dye and antibiotic. *Powder Technology*, **390**, 303–314.

Wang Y.P., Zhang Q.Y., Fang D.Z., Li K.X., Song Z.M., Han W.J. *et al.* (2025b) Selective adsorption of Rb^{+} and Cs^{+} by a superparamagnetic Fe_3O_4@FeMn–MOF from brine. *Desalination*, **600**, 118481.

Wu Q., Feng G., Jiang F., Zhang X., Xu Y., Liu J. *et al.* (2025) Insight into enhanced adsorption of Congo red by petal-like $MgAl_2O_4$: effect of dehydroxylation. *Journal of Physics and Chemistry of Solids*, **197**, 112398.

Yang X.T., Zhou Y., Hu J.J., Zheng Q.W., Zhao Y.P., Lv G.C. & Liao L.B. (2024) Clay minerals and clay-based materials for heavy metals pollution control. *Science of the Total Environment*, **954**, 176193.

Yusuf B.O., Aliyu M., Azeez M.O., Taialla O.A., Lateef S., Sulaimon R. *et al.* (2025) Comprehensive technologies for heavy metal remediation: adsorption, membrane processes, photocatalysis, and AI-driven design. *Desalination*, **615**, 119261.

Zhang H., He Q.D., Zhao W.T., Guo F., Han L. & Wang W.B. (2021a) Superior dyes removal by a recyclable magnetic silicate@Fe_3O_4 adsorbent synthesized from abundant natural mixed clay. *Chemical Engineering Research and Design*, **175**, 272–282.

Zhang H., Fan X., Liu X.Y., He Q.D., Zhao W.T., Han L. *et al.* (2023) Green and cost-efficient functionalized clay adsorbent enables one-step ultraefficient removal of Pb^{2+} at very low and high concentrations. *Applied Clay Science*, **238**, 106934.

Zhang K.G., Liu X., Tan L.C., Xu K.K., Pei W.M., Tang F.K. *et al.* (2025a) Selective electrosorption of trace Pb^{2+} from drinking water by a novel energy-recovery & adsorption-enhanced capacitive deionization system. *Desalination*, **600**, 118518.

Zhang P., Tang L. & Lang C.Y. (2025b) Palygorskite/iron nanoparticles composite for the removal of In(III) from aqueous solutions: characterization, performance, and mechanism. *Applied Clay Science*, **265**, 107678.

Zhang T.T., Wang W., Zhao Y.L., Bai H.Y., Wen T., Kang S.C. *et al.* (2021b) Removal of heavy metals and dyes by clay-based adsorbents: from natural clays to 1D and 2D nano-composites. *Chemical Engineering Journal*, **420**, 127574.

Zhang T.T., Yuan R.L., Zhao A.L., Yin S., Yan H.W., Zhang Z.P. & Geng J.M. (2024) Insight into low-grade natural Linze palygorskite for composite particles preparation towards efficient wastewater treatment. *Colloids and Surfaces A: Physicochemical and Engineering Aspects*, **693**, 134069.

Zhang W.W., Zhao P.J., Pu T.D., Bao W.J., Qie H.T., Tan X. *et al.* (2025c) Enhancing heavy metal immobilization in cropping systems *via* modified clay minerals: a machine learning-assisted meta-analysis. *Journal of Environmental Chemical Engineering*, **13**, 119684.

Zhou S., Zhang X., Pang A.Y., Zhang D.Q., Zhou S.Y., Ma Z. *et al.* (2025) Composite nanocatalysts of amino-organoalkoxysilanes functionalized palygorskite for Knoevenagel condensation reaction. *Applied Clay Science*, **276**, 107941.

Zhu Z.T., Jin X.B., Zhou Y., Hossain M.F., Luo X.B. & Zhou Y.B. (2025) Advancing magnetic chitosan-based materials for sustainable heavy metal removal from water: synthesis, regeneration, and future perspectives. *Separation and Purification Technology*, **377**, 134166.

Zunino F., Boehm-Courjault E. & Scrivener K. (2020) The impact of calcite impurities in clays containing kaolinite on their reactivity in cement after calcination. *Materials and Structures*, **53**, 44.

https://doi.org/10.1180/clm.2026.10049 Published online by Cambridge University Press